

# Precision cosmology with time delay lenses: high resolution imaging requirements

**Xiao-Lei Meng,<sup>1</sup> Tommaso Treu,<sup>1,2</sup> Adriano Agnello,<sup>1,2</sup> Matthew W. Auger,<sup>3</sup> Kai Liao,<sup>1,2</sup> Philip J. Marshall<sup>4</sup>**

<sup>1</sup>Department of Physics, University of California, Santa Barbara, CA 93106, USA

<sup>2</sup>Physics and Astronomy Building, 430 Portola Plaza, Box 951547, Los Angeles, CA 90095-1547, USA

<sup>3</sup>Institute of Astronomy, UK

<sup>4</sup>Kavli Institute for Particle Astrophysics and Cosmology, Stanford University, 452 Lomita Mall, Stanford, CA 94305, USA

E-mail: [xlmeng919@gmail.com](mailto:xlmeng919@gmail.com)

**Abstract.** Gravitational time delays are a powerful probe of cosmology, provided that the gravitational potential of the main deflector can be modeled with sufficient precision. Recent work has shown that this can be achieved by detailed modeling of the host galaxies of lensed quasars. The distortion of the images as measured over large number of pixels provides tight constraints on the difference between the gravitational potential between the two quasars, and thus on cosmology in combination with the measured time delay. We carry out a systematic exploration of the high resolution imaging required to exploit the thousands of lensed quasars that will be discovered by current and upcoming surveys with the next decade. Specifically we simulate realistic lens systems as imaged by the Hubble Space Telescope (HST), James Webb Space Telescope (JWST), ground based adaptive optics images taken with Keck or the Thirty Meter Telescope (TMT). We compare the performance of these pointed observations with that of images taken by the Euclid-VIS, Wide-Field Infrared Survey Telescope (WFIRST) and Large Synoptic Survey Telescope (LSST) surveys. Using as our metric the precision with which the slope of the mass density profile for the main deflector can be measured **we find that...**

---

## Contents

<b>1</b>	<b>Introduction</b>	<b>1</b>
<b>2</b>	<b>Instrument Simulations</b>	<b>1</b>
<b>3</b>	<b>The Lens Sample</b>	<b>3</b>
<b>4</b>	<b>Lens Reconstruction</b>	<b>3</b>
<b>5</b>	<b>Results</b>	<b>4</b>
<b>6</b>	<b>Summary</b>	<b>4</b>

---

## 1 Introduction

[TT to put introfirst here; introduce ‘informative pixels’ that will be referred to in Sect.s 2 and 3; mention that we’re basically observing how radial magnification changes across the lens, so that we need to understand how that is affected by PSF, pixel-size, and S/N ratio.]

In the past few years, gravitational time delays have emerged as a...

This paper is organized as follows. We first introduce a variety of instrument informations in Section 2. Next, we briefly summarize the lens sample used in this work in Section 3 and show how to reconstruct lens models as imaged by these instruments in Section 4. The results from simulation in Section 5. Finally, we discuss and summarize our work in Section 6. Throughout this paper, all magnitudes are given in the AB system. Even though it is not crucial to our findings, we adopt a spatially flat  $\Lambda$ CDM cosmology with  $\Omega_m = 0.3$ ,  $\Omega_\Lambda = 0.7$ , and the Hubble constant  $H_0 = 70 \text{ km s}^{-1} \text{ Mpc}^{-1}$  when calculating distances.

## 2 Instrument Simulations

The way a lens is observed and modelled, whence the parameter uncertainties, are influenced fundamentally by the instrumental setup itself. First, the signal-to-noise depends on the exposure-time adopted, sky or background noise in a chosen band, and the instrumental readout noise. Second, the pixel-size and the point-spread function (PSF) properties determine how finely one can map the system being observed, hence how robustly the deflections on either side of the lens can be quantified.

Here we illustrate the main properties of instruments that will be considered in the simulations. For the sake of completeness, they can either be ground-based or space-based telescopes, or even cadenced surveys where the total exposure cannot set arbitrarily. Table 1 and figure 1 display the main properties of the telescopes that are needed when generating images of mock gravitational lenses. Figure 2[XLM, can you do it? Sure! have done!] shows the typical PSF of each instrument.

1. HST. The Advanced Camera for Surveys (ACS) is a third-generation HST instrument with a scale of  $0.05''/\text{pixel}$ . Its properties used are taken from Space Telescope Science Institute and HST Exposure Time Calculator<sup>1</sup>. We are interested in F814W band.

2. JWST. JWST is a infrared-optimized space telescope which obtains four instruments: near-infrared camera, mid-infrared instrument, near-infrared multi-object spectrograph, and a tunable filter

---

<sup>1</sup><http://etc.stsci.edu>

imager. Its scientific goals include exploring planetary systems, star evolution, galaxy-scale theme, and remote dark ages (Gardner et al. 2006 [1]). We determinate instrument properties by JWST Exposure Time Calculator <sup>2</sup>. F200W band is selected to consider. The pixel size is 0.032''/pixel. Zero point, readout noise, and background noise are calculated from count rates at fixed exposure time.

3. Keck (LGSAO & NGSAO). Keck Observatory's next-generation adaptive optics (NGAO) is designed to discover important astrophysics problems, for example, dark matter distribution in the Milky Way, galaxy evolution study, general relativity affection at galactic center, the origin and evolution of nearby planetary systems (Wizinowich et al. 2010 [2]). But, when existing bright background stars in the sky

According to the informations given by Keck NIRC2 Observer's Manual <sup>3</sup>, properties of Keck can be deduced, both with LGSAO and NGSAO. Here, we choose MCDS as the readout mode of the detector, meanwhile read number  $N = 16$ . The pixel size is 0.01''/pixel.

4. TMT. IRIS is a instrument with the imaging and infrared (0.85 - 2.5 micron) integral field spectrograph abilities for TMT. Based on a primary spectral resolution of 4000 and more accurate pixel-size 0.004'', the instrument has the advantage in many fields, from star forming regions to high-redshift galaxy and galactic center study (Larkin et al. 2010 [3]). The selected filter's zero point and background noise are obtained according to a prospect work (Do et al. 2014 [4]). Using TMT ETC <sup>4</sup>, readout noise can be calculated (please note that the total efficiency is around 0.4 in ETC).

5. Euclid. This is a space survey telescope designed by the European Space Agency. Euclid has two instruments: a high-resolution visible imager, and a NIR imaging instrument. It aims to investigate the nature of dark energy, dark matter, and gravity by using cosmological probes, such as weak gravitational lensing and baryon acoustic oscillations (Laureijs et al. 2011). The instrument properties are taken from Schweitzer et al. 2010 [5], Penny et al. 2013 [6] and Cropper et al. 2014 [7]. The readout noise depends on the number of non-destructive reads. The pixel size is 0.1''/pixel.

6. WFIRST. As a wild field of view and low-resolution spectroscopy observatory, WFIRST with the infrared detector technology is expected to contribute to the following goals in astrophysics: planetary systems in the Milky Way; reionization epoch history by high redshift quasars at  $z > 10$ ; and the study of dark energy and modifications to Einstein's gravity (Green et al. 2012 [8]). We are interested in the HLS Imaging survey, F184W filter. The pixel size is 0.11''/pixel. The properties are presumed based on WFIRST-Astrophysics Focused Telescope Assets Final Report (by the Science Definition Team (ADT) and WFIRST Project) and WFIRST Exposure Time Calculator <sup>5</sup>.

7. LSST. LSST is designed to imaging surveys in the optical bands (out to  $\sim 1$  micron). It is dedicated with dramatic advances across main astrophysics themes: the nature of dark energy and dark matter; optical sky survey to get the data products such as gamma-ray burst, optical bursters, gravitational micro-lensing, new populations of novae and supernova, stellar tidal disruptions and so on; the structure of the Milky Way; and the Solar System exploring (Ivezic et al. 2008 [9]). As discussed by Ivezic et al. 2008 and LSST Science Requirements Document <sup>6</sup>, LSST properties can be deduced. The pixel size is 0.2''/pixel.

For modeling the light of the lens galaxies, the lensed background source, and the lensed point source, we use realistic PSFs for HST, JWST, Keck (LGSAO & NGSAO), and TMT getting from stars in the field which has been proved to be a effective method when modeling galaxy-scale strong lenses

---

<sup>2</sup><http://jwstetc.stsci.edu>

<sup>3</sup><http://www2.keck.hawaii.edu/inst/nirc2/Manual/ObserversManual.html#Section2.2>

<sup>4</sup>[http://tmt.mtk.nao.ac.jp/ETC\\_readme.html](http://tmt.mtk.nao.ac.jp/ETC_readme.html)

<sup>5</sup><http://wfirfirst-web.ipac.caltech.edu/wfDepc/wfDepc.jsp?etc>

<sup>6</sup><http://www.lsst.org/files/docs/SRD.pdf>

(Marshall et al. 2007 [10]; Suyu et al. 2009 [11]). On the other hand, for Euclid, WFIRST, and LSST, Gaussian PSFs are adopted to generate mock data in this work by lack of sufficient information. Full width at half maximum (FWHM) of PSF with selected filter are

**For TT:** A sentence or two on HST and ACS; similarly for JWST (what it's planned to do and when it's expected to start); similarly for TMT and IRIS; Keck, both with LGSAO and NGSAO and why we must consider both; then Euclid, WFIRST, LSST.

### 3 The Lens Sample

We have chosen four prototypical systems for this exploration, characterized as *faint* or **bright** and **double** or **quad** depending on the photometry and image configuration. Their structural parameters are listed in Table 2. This set of four main choices covers regimes with different numbers of informative pixels, which depend on the S/N ratio and on the number of images produced by the lens.

To remain as realistic as possible, the mocks are based upon lenses in the SLACS (...) and SL2S (...) samples. When not explicitly known from existing data, mock model parameters are assigned via plausibility arguments as specified below. The source and deflector of the *bright* configurations are built along SLACS J0330-0020 as modelled by **Auger et al.(SLACS11)**. For the *faint* configuration, the deflector has parameters from the **Sonnenfeld et al. (????)** model of SL2S J135949+553550. Source magnitudes in the *faint* case are arbitrarily set to 25.0 in all bands, whence the source effective radius  $R_{eff}$  is assigned along the size-magnitude relation given by **Newton et al. (2011?)**. In all cases, the source positions are assigned so as to map the source in either two or four images. Unknown magnitudes in *K* band are assigned from *H*-band ones via  $K_{AB} = H_{AB}$ .

**Question:** What are the point-source magnitudes, even if they're not specifically modelled? How were they assigned? (They are in the Table 4. For the fainter systems, they are all 24.0 for all the filters except for TMT. The magnitude of point source is 26.0 for TMT, that's because TMT has an amazing detecting ability. For the brighter systems, they are assigned with magnitude of source galaxy - 0.5 for filter K, VIS, and H; - 1.0 for filter I.) Based on the recipe that Kai and I assembled? Also, magnitudes in the tables are not necessarily the instrument ones, how are they converted? With the XLM's template-based table from AA or something different? (For fainter systems, lens magnitude for I filter is from Ale's paper III, mag for K filter is estimated by TT based on the other colors, mag for VIS filter is evaluated by  $mag(r, i, z) = -2.5 * log((10^{-0.4r} + 10^{-0.4i} + 10^{-0.4z})/2)$  (there are r, i, z filters informations in Ale's paper III),  $H_{AB} = K_{AB}$ . For brighter systems, lens mag for I filter and V filter are from Auger's paper; mag for K band is determined by TT;  $H_{AB} = K_{AB}$ ) (For fainter systems, the source galaxy magnitude for filters are all 25.0 which is determined by TT. For brighter systems, the source galaxy magnitude for I and V filters are from Newton's paper, the source galaxy magnitude for K filter is 22.0 which is determined by TT)

Then: say that source is mapped onto lens plane with formalism illustrated later on, lens light is summed to it, noise added. Refer to one example of puppies, **including TMT with kernel smoothing.**

### 4 Lens Reconstruction

Here we describe how the mock lens models are generated, using power-law lenses. The reader familiar with this topic can easily skip to the next Section.

The deflector's mass profile is assigned within a class of power-law models,

$$\Sigma(x, y) = \Sigma_0(qX^2 + q^{-1}Y^2)^{-\gamma'}, \quad (4.1)$$

where the  $\{X, Y\}$  axes are rotated by some position angle w.r.to the canonical  $x$  (increasing to the West) and  $y$  (increasing to the North). This means that the  $\{X, Y\}$  deflections scale as ..., where  $g(\theta)$  a just function of the relative angle west-of-north. Fast methods to compute deflections from power-law profiles have been given by **Barkana** (????). Power-law models of elliptical galaxies **Evans** (1994?) have often been used with success over the years to model gravitational lenses [**references!**]. In utter generality, the lensing deflections are given by

$$\dots \quad (4.2)$$

where

$$\Sigma_{cr} = \dots \quad (4.3)$$

encompasses the relative positions of source, deflector and observer. Then, in our power-law case the deflections can be rewritten conveniently as

$$\dots \quad (4.4)$$

This introduces the Einstein radius  $R_E$ , which is such that in the spherical case ( $q = 1$ ) the mean dimensionless density  $\langle \Sigma \rangle / \Sigma_{cr}$  within a circle of radius  $R_E$  is exactly 1. This is also the radius of a ring traced by the host of the quasar when this is exactly aligned with the lens galaxy.

Lensed image profiles are obtained by Inverse Ray Shooting:.. First, each pixel position in the image plane is mapped back to the source plane via the deflections in eq ... Then, we exploit the fact that surface-brightness is preserved by lensing, i.e.

$$\dots \quad (4.5)$$

In general, when dealing with more complex caustics from substructure **Vegetti** (????) or microlensing **Mediavilla** (????), rays are shot through an adaptive, triangular tessellation in the image place. Here, we can simply use a rectangular grid in the image-plane to obtain sufficiently accurate results.

The same code is used to generate the mock models and to fit them. The model fits the following parameters: **which ones?** Goodness of fit is assessed through the image-plane  $\chi^2$ , comparing the model and mock data surface brightness profiles. The quasar images are not used in the fit, which is performed just on the lensed host. This is because in reality, even in the absence of substructure lensing, the relative fluxes of the point-like images of the quasar can be appreciably affected by microlensing or dust lanes in the foreground. Uncertainties are obtained via MCMC exploration of the likelihood, which in this case is simply given by  $\mathcal{L} \propto \exp[-\chi^2/2]$ .

## 5 Results

## 6 Summary

## Acknowledgments

## References

- [1] J. P. Gardner, J. C. Mather, M. Clampin, R. Doyon, M. A. Greenhouse, H. B. Hammel, J. B. Hutchings, P. Jakobsen, S. J. Lilly, K. S. Long, J. I. Lunine, M. J. McCaughean, M. Mountain, J. Nella, G. H. Rieke, M. J. Rieke, H.-W. Rix, E. P. Smith, G. Sonneborn, M. Stiavelli, H. S. Stockman, R. A. Windhorst, and G. S. Wright, *The James Webb Space Telescope*, Space Sci. Rev. **123** (Apr., 2006) 485–606, [[astro-ph/0606175](#)].

- [2] P. Wizinowich, S. Adkins, R. Dekany, D. Gavel, C. Max, R. Bartos, J. Bell, A. Bouchez, J. Chin, A. Conrad, A. Delacroix, E. Johansson, R. Kupke, C. Lockwood, J. Lyke, F. Marchis, E. McGrath, D. Medeiros, M. Morris, D. Morrison, C. Neyman, S. Panteleev, M. Pollard, M. Reinig, T. Stalcup, S. Thomas, M. Troy, K. Tsubota, V. Velur, K. Wallace, and E. Wetherell, *W. M. Keck Observatory's next-generation adaptive optics facility*, in *Society of Photo-Optical Instrumentation Engineers (SPIE) Conference Series*, vol. 7736 of *Society of Photo-Optical Instrumentation Engineers (SPIE) Conference Series*, p. 0, July, 2010.
- [3] J. E. Larkin, A. M. Moore, E. J. Barton, B. Bauman, K. Bui, J. Canfield, D. Crampton, A. Delacroix, M. Fletcher, D. Hale, D. Loop, C. Niehaus, A. C. Phillips, V. Reshetov, L. Simard, R. Smith, R. Suzuki, T. Usuda, and S. A. Wright, *The infrared imaging spectrograph (IRIS) for TMT: instrument overview*, in *Society of Photo-Optical Instrumentation Engineers (SPIE) Conference Series*, vol. 7735 of *Society of Photo-Optical Instrumentation Engineers (SPIE) Conference Series*, p. 29, July, 2010. [arXiv:1007.1973](https://arxiv.org/abs/1007.1973).
- [4] T. Do, S. A. Wright, A. J. Barth, E. J. Barton, L. Simard, J. E. Larkin, A. M. Moore, L. Wang, and B. Ellerbroek, *Prospects for Measuring Supermassive Black Hole Masses with Future Extremely Large Telescopes*, Astron. J. **147** (Apr., 2014) 93, [[arXiv:1401.7988](https://arxiv.org/abs/1401.7988)].
- [5] M. Schweitzer, R. Bender, R. Katterloher, F. Eisenhauer, R. Hofmann, R. Saglia, R. Holmes, O. Krause, H.-W. Rix, J. Booth, P. Fagrelius, J. Rhodes, S. Seshadri, A. Refregier, J. Amiaux, J.-L. Augueres, O. Boulade, C. Cara, A. Amara, S. Lilly, E. Atad-Ettedgui, A.-M. di Giorgio, L. Duvet, C. Kuehl, and M. Syed, *NIP: the near infrared imaging photometer for Euclid*, in *Society of Photo-Optical Instrumentation Engineers (SPIE) Conference Series*, vol. 7731 of *Society of Photo-Optical Instrumentation Engineers (SPIE) Conference Series*, p. 1, July, 2010.
- [6] M. T. Penny, E. Kerins, N. Rattenbury, J.-P. Beaulieu, A. C. Robin, S. Mao, V. Batista, S. Calchi Novati, A. Cassan, P. Fouqué, I. McDonald, J. B. Marquette, P. Tisserand, and M. R. Zapatero Osorio, *ExELS: an exoplanet legacy science proposal for the ESA Euclid mission - I. Cold exoplanets*, Mon. Not. R. Astron. Soc. **434** (Sept., 2013) 2–22, [[arXiv:1206.5296](https://arxiv.org/abs/1206.5296)].
- [7] M. Cropper, S. Pottinger, S.-M. Niemi, J. Denniston, R. Cole, M. Szafraniec, Y. Mellier, M. Berthé, J. Martignac, C. Cara, A. M. di Giorgio, A. Sciortino, S. Paltani, L. Genolet, J.-J. Fourmand, M. Charra, P. Guttridge, B. Winter, J. Endicott, A. Holland, J. Gow, N. Murray, D. Hall, J. Amiaux, R. Laureijs, G. Racca, J.-C. Salvignol, A. Short, J. Lorenzo Alvarez, T. Kitching, H. Hoekstra, and R. Massey, *VIS: the visible imager for Euclid*, in *Society of Photo-Optical Instrumentation Engineers (SPIE) Conference Series*, vol. 9143 of *Society of Photo-Optical Instrumentation Engineers (SPIE) Conference Series*, p. 0, Aug., 2014.
- [8] J. Green, P. Schechter, C. Baltay, R. Bean, D. Bennett, R. Brown, C. Conselice, M. Donahue, X. Fan, B. S. Gaudi, C. Hirata, J. Kalirai, T. Lauer, B. Nichol, N. Padmanabhan, S. Perlmutter, B. Rauscher, J. Rhodes, T. Roellig, D. Stern, T. Sumi, A. Tanner, Y. Wang, D. Weinberg, E. Wright, N. Gehrels, R. Sambruna, W. Traub, J. Anderson, K. Cook, P. Garnavich, L. Hillenbrand, Z. Ivezić, E. Kerins, J. Lunine, P. McDonald, M. Penny, M. Phillips, G. Rieke, A. Riess, R. van der Marel, R. K. Barry, E. Cheng, D. Content, R. Cutri, R. Goullioud, K. Grady, G. Helou, C. Jackson, J. Kruk, M. Melton, C. Peddie, N. Rioux, and M. Seiffert, *Wide-Field InfraRed Survey Telescope (WFIRST) Final Report*, ArXiv e-prints (Aug., 2012) [[arXiv:1208.4012](https://arxiv.org/abs/1208.4012)].
- [9] Z. Ivezić, J. A. Tyson, B. Abel, E. Acosta, R. Allsman, Y. AlSayyad, S. F. Anderson, J. Andrew, R. Angel, G. Angeli, R. Ansari, P. Antilogus, K. T. Arndt, P. Astier, E. Aubourg, T. Axelrod, D. J. Bard, J. D. Barr, A. Barrau, J. G. Bartlett, B. J. Bauman, S. Beaumont, A. C. Becker, J. Becla, C. Beldica, S. Bellavia, G. Blanc, R. D. Blandford, J. S. Bloom, J. Bogart, K. Borne, J. F. Bosch, D. Boutigny, W. N. Brandt, M. E. Brown, J. S. Bullock, P. Burchat, D. L. Burke, G. Cagnoli, D. Calabrese, S. Chandrasekharan, S. Chesley, E. C. Cheu, J. Chiang, C. F. Claver, A. J. Connolly, K. H. Cook, A. Cooray, K. R. Covey, C. Cribbs, W. Cui, R. Cutri, G. Daubard, G. Daues, F. Delgado, S. Digel, P. Doherty, R. Dubois, G. P. Dubois-Felsmann, J. Durech, M. Eracleous, H. Ferguson, J. Frank, M. Freemon, E. Gangler, E. Gawiser, J. C. Geary, P. Gee, M. Geha, R. R. Gibson, D. K. Gilmore,

T. Glanzman, I. Goodenow, W. J. Gressler, P. Gris, A. Guyonnet, P. A. Hascall, J. Haupt, F. Hernandez, C. Hogan, D. Huang, M. E. Huffer, W. R. Innes, S. H. Jacoby, B. Jain, J. Jee, J. G. Jernigan, D. Jevremovic, K. Johns, R. L. Jones, C. Juramy-Gilles, M. Juric, S. M. Kahn, J. S. Kalirai, N. Kallivayalil, B. Kalmbach, J. P. Kantor, M. M. Kasliwal, R. Kessler, D. Kirkby, L. Knox, I. Kotov, V. L. Krabbendam, S. Krughoff, P. Kubanek, J. Kuczewski, S. Kulkarni, R. Lambert, L. Le Guillou, D. Levine, M. Liang, K. Lim, C. Lintott, R. H. Lupton, A. Mahabal, P. Marshall, S. Marshall, M. May, R. McKercher, M. Migliore, M. Miller, D. J. Mills, D. G. Monet, M. Moniez, D. R. Neill, J. Nief, A. Nomerotski, M. Nordby, P. O'Connor, J. Oliver, S. S. Olivier, K. Olsen, S. Ortiz, R. E. Owen, R. Pain, J. R. Peterson, C. E. Petry, F. Pierfederici, S. Pietrowicz, R. Pike, P. A. Pinto, R. Plante, S. Plate, P. A. Price, M. Prouza, V. Radeka, J. Rajagopal, A. Rasmussen, N. Regnault, S. T. Ridgway, S. Ritz, W. Rosing, C. Roucelle, M. R. Rumore, S. Russo, A. Saha, B. Sassolas, T. L. Schalk, R. H. Schindler, D. P. Schneider, G. Schumacher, J. Sebag, G. H. Sembroski, L. G. Seppala, I. Shipsey, N. Silvestri, J. A. Smith, R. C. Smith, M. A. Strauss, C. W. Stubbs, D. Sweeney, A. Szalay, P. Takacs, J. J. Thaler, R. Van Berg, D. Vanden Berk, K. Vetter, F. Virieux, B. Xin, L. Walkowicz, C. W. Walter, D. L. Wang, M. Warner, B. Willman, D. Wittman, S. C. Wolff, W. M. Wood-Vasey, P. Yoachim, H. Zhan, and for the LSST Collaboration, *LSST: from Science Drivers to Reference Design and Anticipated Data Products*, ArXiv e-prints (May, 2008) [[arXiv:0805.2366](#)].

- [10] P. J. Marshall, T. Treu, J. Melbourne, R. Gavazzi, K. Bundy, S. M. Ammons, A. S. Bolton, S. Burles, J. E. Larkin, D. Le Mignant, D. C. Koo, L. V. E. Koopmans, C. E. Max, L. A. Moustakas, E. Steinbring, and S. A. Wright, *Superresolving Distant Galaxies with Gravitational Telescopes: Keck Laser Guide Star Adaptive Optics and Hubble Space Telescope Imaging of the Lens System SDSS J0737+3216*, *Astrophys. J.* **671** (Dec., 2007) 1196–1211, [[arXiv:0710.0637](#)].
- [11] S. H. Suyu, P. J. Marshall, R. D. Blandford, C. D. Fassnacht, L. V. E. Koopmans, J. P. McKean, and T. Treu, *Dissecting the Gravitational Lens B1608+656. I. Lens Potential Reconstruction*, *Astrophys. J.* **691** (Jan., 2009) 277–298, [[arXiv:0804.2827](#)].

**Table 1.** Telescope Properties

Telescope	Instrument	Filter	Zero Point	Readout Noise (e <sup>-</sup> /pixel/s)	Background Noise (e <sup>-</sup> /pixel/s)	Pixel Size (arcsec)
HST	ACS	F814W	25.94	4.20	0.11	0.050
JWST	NIRCAM	F200W	27.85	9.00	0.20	0.032
Keck	NIRC2/NGSAO	<i>K'</i>	28.04	5.75	25.94	0.010
TMT	IRIS	nIR	31.10	2.00	21.20	0.004
Euclid	VIS	<i>r + i + z</i>	25.58	4.50	0.43	0.100
WFIRST	DRM(?)	F184	26.18	5.00	0.11	0.110
LSST	—	<i>I</i>	28.35	5.00	68.00	0.200

Observational facilities (telescopes or cadenced surveys) considered in this work. Zero points are given in the ABmag system. The near-IR wavelength coverage of IRIS is  $0.85 - 2.5 \mu\text{m}$ , the VIS imager of Euclid spans the whole  $r + i + z$  wavelength range.

**Table 2.** Surface Brightness Profile Models

Lens Name	$R_{\text{eff}}$ (arcsec)	$q$	P.A. (deg)	$n$	$\Delta x$ (arcsec)	$\Delta y$ (arcsec)	$m_I$	$m_K$	$m_{\text{VIS}}$	$m_H$
Parameters for the Source										
fainter system <sup>a</sup>	0.23	0.92	54.0	4.0	0.0662	-0.167	25.0	25.0	25.0	25.0
fainter system <sup>b</sup>	0.23	0.92	54.0	4.0	0.008	0.298	25.0	25.0	25.0	25.0
brighter system <sup>b</sup>	0.12	0.77	120.0	1.33	-0.195	0.34	22.73	22.0	23.46	22.0
brighter system <sup>a</sup>	0.12	0.77	120.0	1.33	0.01	-0.005	22.73	22.0	23.46	22.0
Parameters for the lens										
fainter system	1.76	0.61	-9.6	4.0	—	—	20.69	19.7	21.13	19.7
brighter system	0.91	0.81	113.2	4.0	—	—	17.99	16.5	18.84	16.5

The effective radius  $R_{\text{eff}}$  is the radius at which the major axis contains half of the total flux.  $q$  denotes the axis ratio. P.A. is with respect to the x-axis. The Sérsic index  $n$  controls the degree of curvature of the galaxy light profile. Magnitudes  $m$  are given in the ABmag system. The only difference among sources of different brightness is in the source-position, which is set to produce either two or four images.

<sup>a</sup> 4 QSO images exist in the lens plane.

<sup>b</sup> 2 QSO images exist in the lens plane.

**Table 3.** Lens Model Parameters

Lens Name	$z$	$R_{\text{Ein}}$ (arcsec)	$q$	P.A. (deg)	$\gamma'$
fainter system	0.783	1.14	0.6	14.7	2.0
brighter system	0.351	1.1	0.81	113.2	2.0

**Rephrase**[ $R_{\text{Ein}}$  is the radius of a ring which is taken from a lensing phenomenon if a point source is located on the viewing direction extending from the observer].  $q$  denotes the axis ratio. P.A. is anti-clockwise from the x-axis. The underlying deflector is a Singular Isothermal Ellipsoid ( $\gamma'=2$ ), which will be fit using power-law models.

<sup>a</sup> 4 QSO images exist in the lens plane.

<sup>b</sup> 2 QSO images exist in the lens plane.

**Table 4.** Point Source Parameters

Lens Name	magnitude (I)	magnitude (K)	magnitude (VIS)	magnitude (H)	magnification (I)	magnification (II)	magnification (III)	magnification (IV)
fainter system <sup>a</sup>	24.0	24.0	24.0	24.0	2.84	3.75	6.59	2.78
fainter system <sup>b</sup>	24.0	24.0	24.0	24.0	2.78	2.48	—	—
brighter system <sup>b</sup>	21.7	21.5	22.9	21.5	1.22	6.10	—	—
brighter system <sup>a</sup>	21.7	21.5	22.9	21.5	6.09	8.22	6.86	7.53

Magnitude m is given in the ABmag system.

<sup>a</sup> 4 QSO images exist in the lens plane.

<sup>b</sup> 2 QSO images exist in the lens plane.

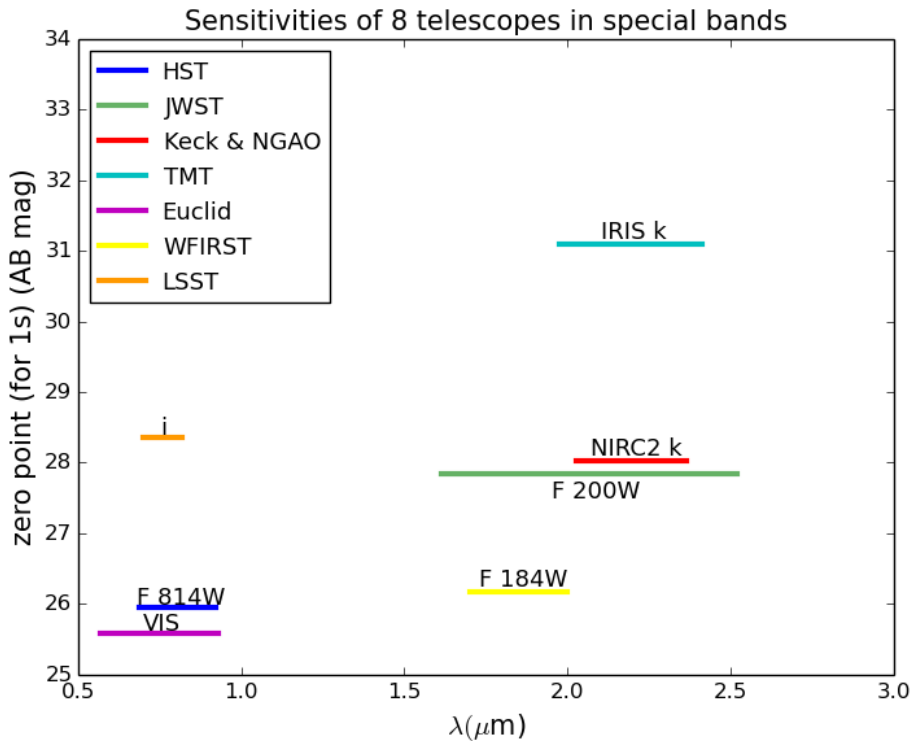


**Figure 1.** Zero Points in AB magnitudes of HST (blue), JWST (green), Keck & NGAO (red), TMT (cyan), Euclid (magenta), WFIRST (yellow) and LSST (orange) in units of per second. Different color bars indicate the wavelength range of each telescope used in this work.

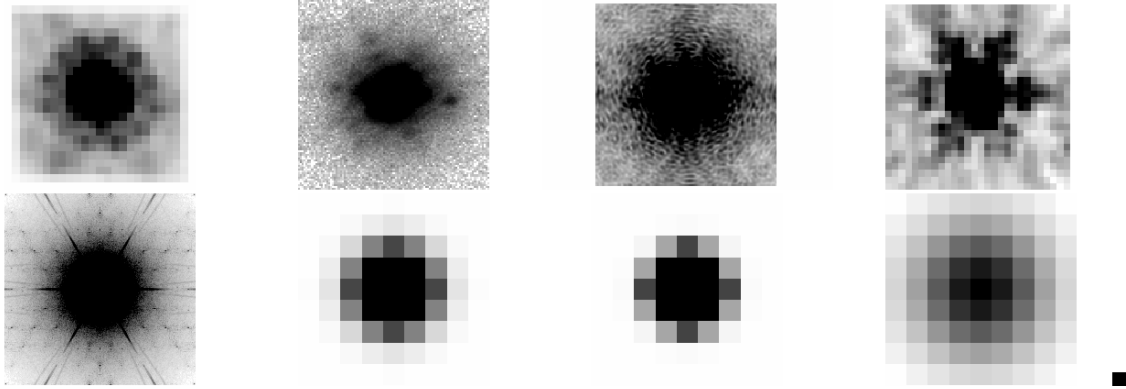


**Figure 2.** Gaussian PSF are used for Euclid, WFIRST, and LSST.

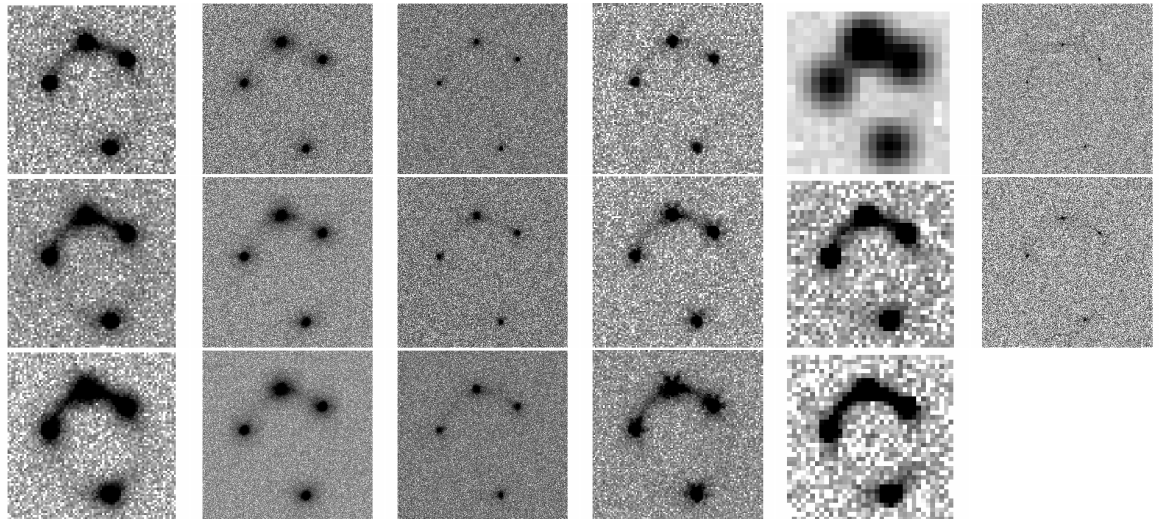


**Figure 3.** Simulated lens system results showing the fainter lens system (4 QSO images in the lens plane). The simulated image pixel scales are all  $4'' \times 4''$ . The first 4 columns, from left to right, represent HST, Keck, NGAO, and JWST; from top to bottom, correspond to  $1/3 \times$  good exposure time, good exposure time, and  $3 \times$  good exposure time ( See the definition of “good exposure time” in Section \*.\*). The fifth column include 3 survey detections by 3 different telescopes, from top to bottom, for LSST, Euclid, and WFIRST respectively. The last column is for TMT with 2 fixed exposure time: 360 seconds and 1080 seconds.

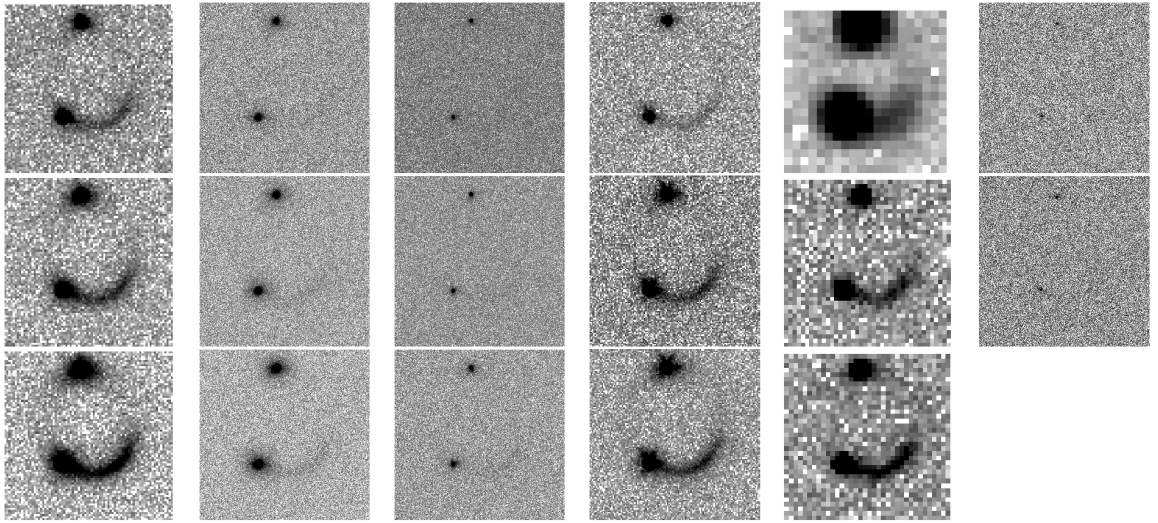


**Figure 4.** Same as Fig. 2, except that the simulated lens system results showing the fainter lens system (2 QSO images in the lens plane).

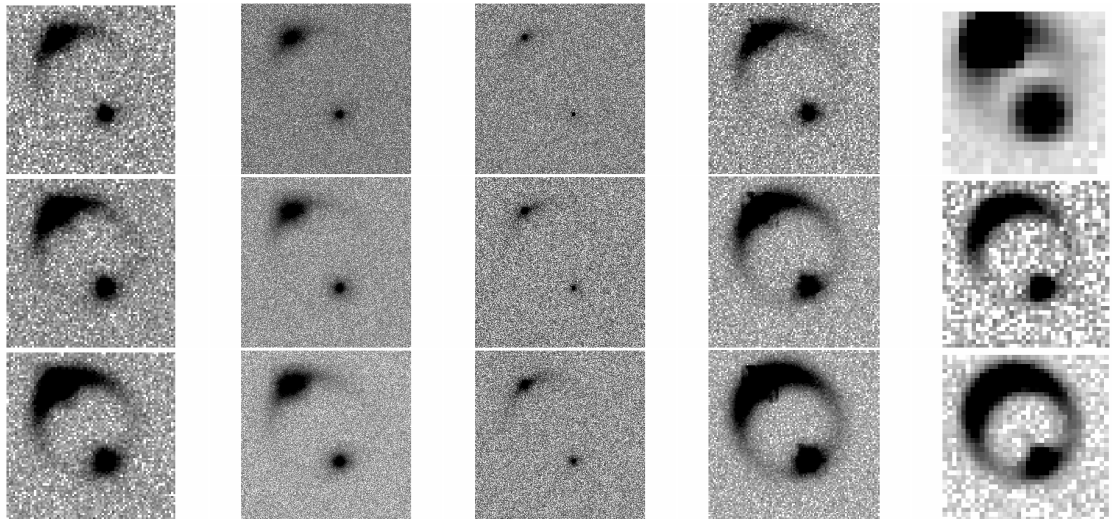


**Figure 5.** Simulated lens system results showing the brighter lens system (2 QSO images in the lens plane). The simulated image pixel scales are all  $4'' \times 4''$ . The first 3 columns, from left to right, present HST, Keck, and NGAO; from top to bottom, correspond to  $1/3 \times$  good exposure time, good exposure time, and  $3 \times$  good exposure time. The fourth column shows JWST with 3 fixed exposure time: 60 seconds, 180 seconds, and 540 seconds. The last column include 3 survey detections by 3 different telescopes, from top to bottom, for LSST, Euclid, and WFIRST respectively.

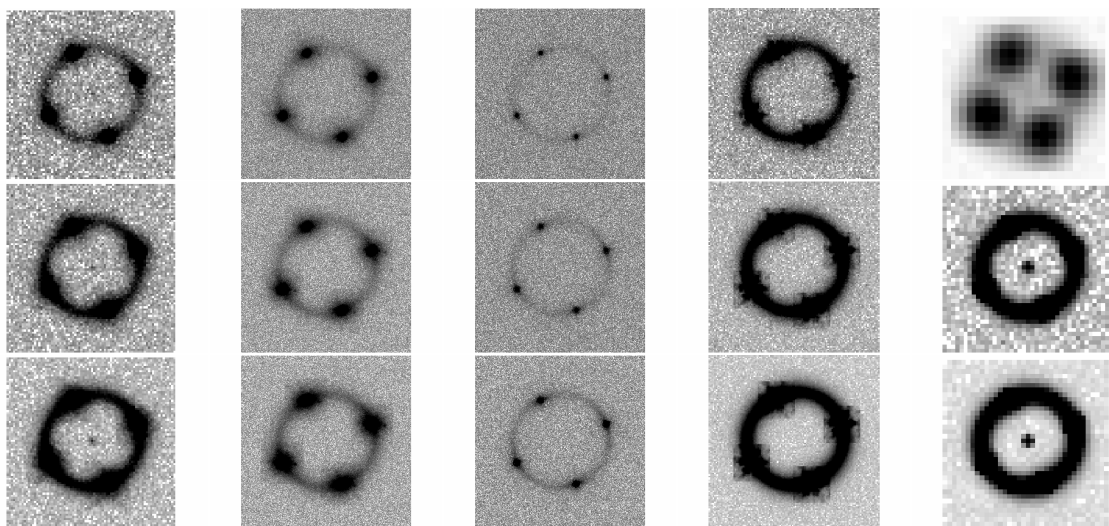


**Figure 6.** Same as Fig. 4, except that the simulated lens system results showing the brighter lens system (4 QSO images in the lens plane). The black spots in the center of the simulated images using HST, Euclid and WFIRST are from the efforts of strong signal pixels, so it's a “ghost” image which can be ignored.

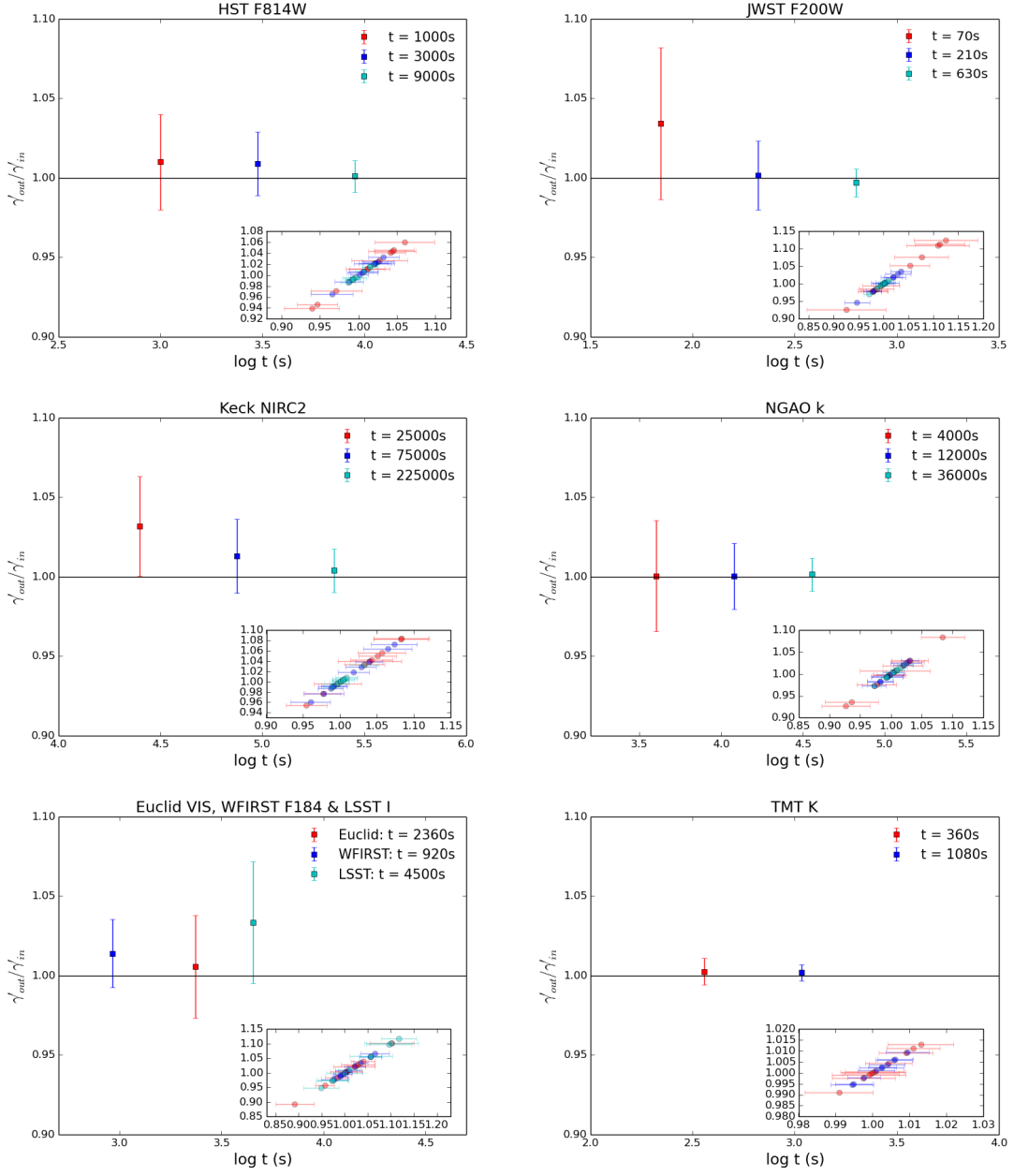


**Figure 7.** The ability of recovering mass slope with respect to different exposure time for a variety of telescopes. This figure shows the fainter lens system with 4 QSO images in the lens plane.  $\gamma'_{in}$  is the input SIE mass slope.  $\gamma'_{out}$  is drawn from MCMC sampling based on the simulated images given  $\gamma'_{in}$ . The error bar represents  $1\sigma$  confidence range. The insert in each panel shows all 10 simulation results for each exposure time with the same color coding. Note that both axes represent  $\gamma'_{out}/\gamma'_{in}$  whereas error bars are only shown on the x-axis for clarity.

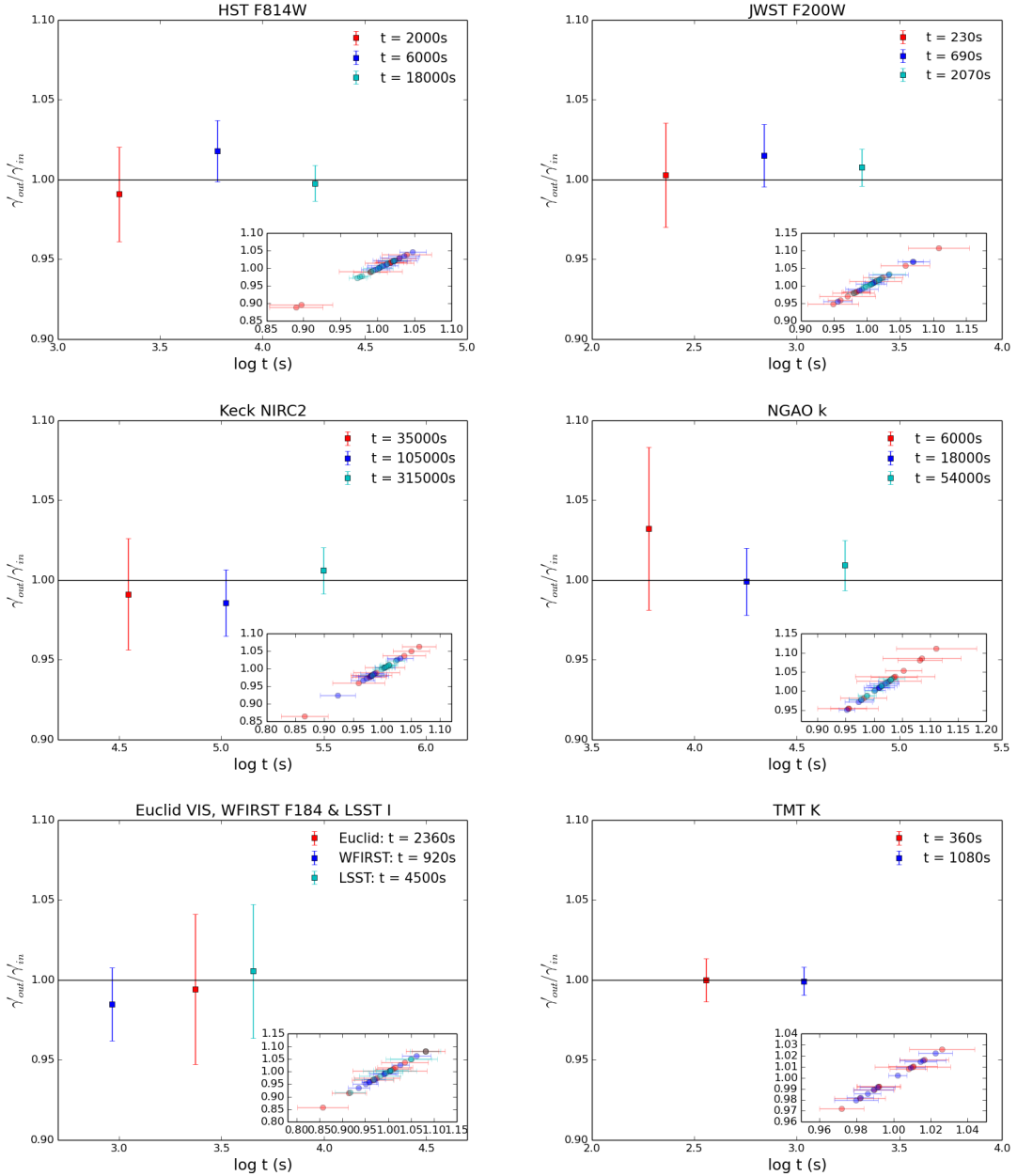


**Figure 8.** Same as Fig. 6, except that this figure is shown for the fainter lens system with 2 QSO images in the lens plane.

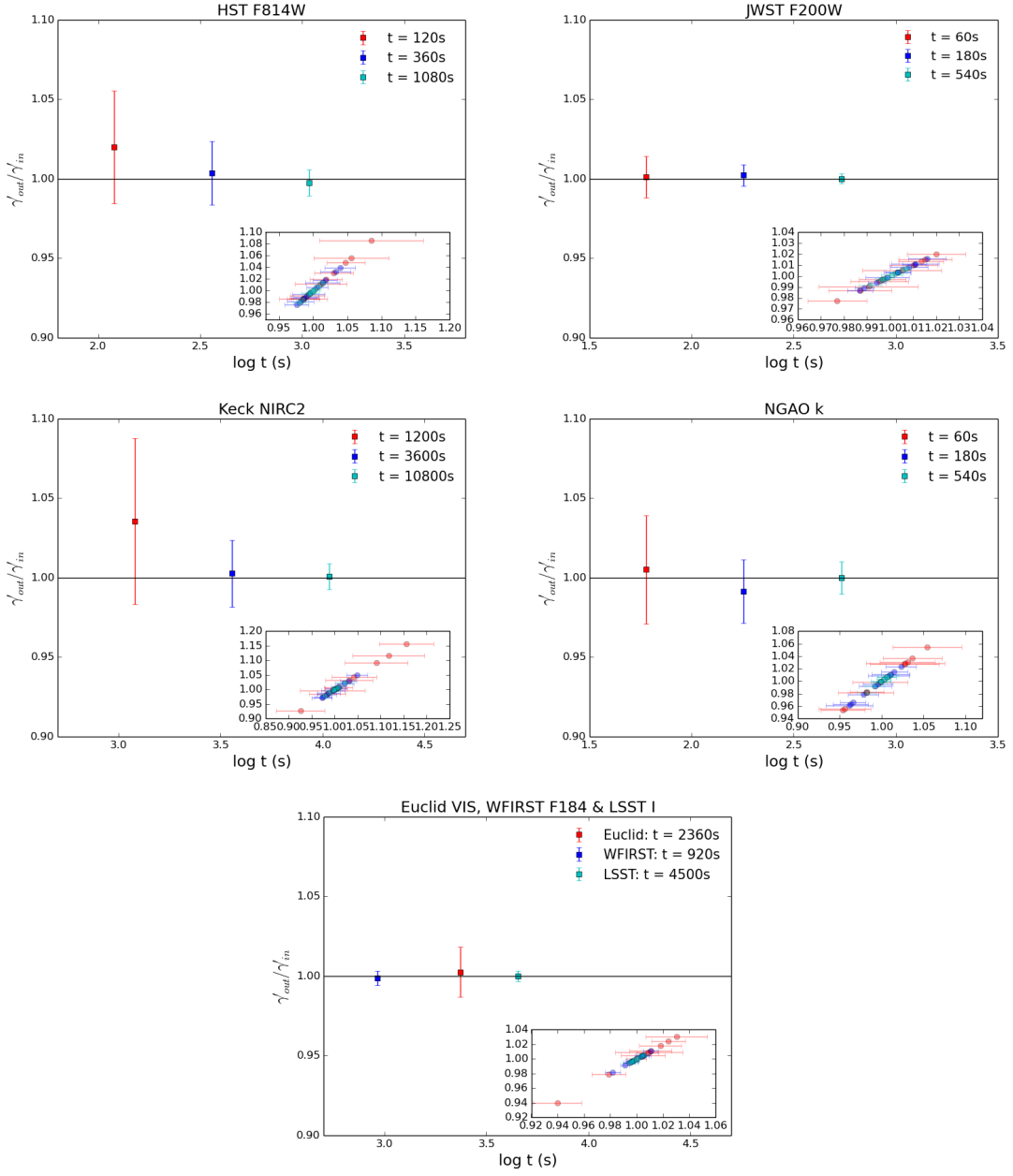


**Figure 9.** Same as Fig. 6, except that this figure is shown for the brighter lens system with 2 QSO images in the lens plane.

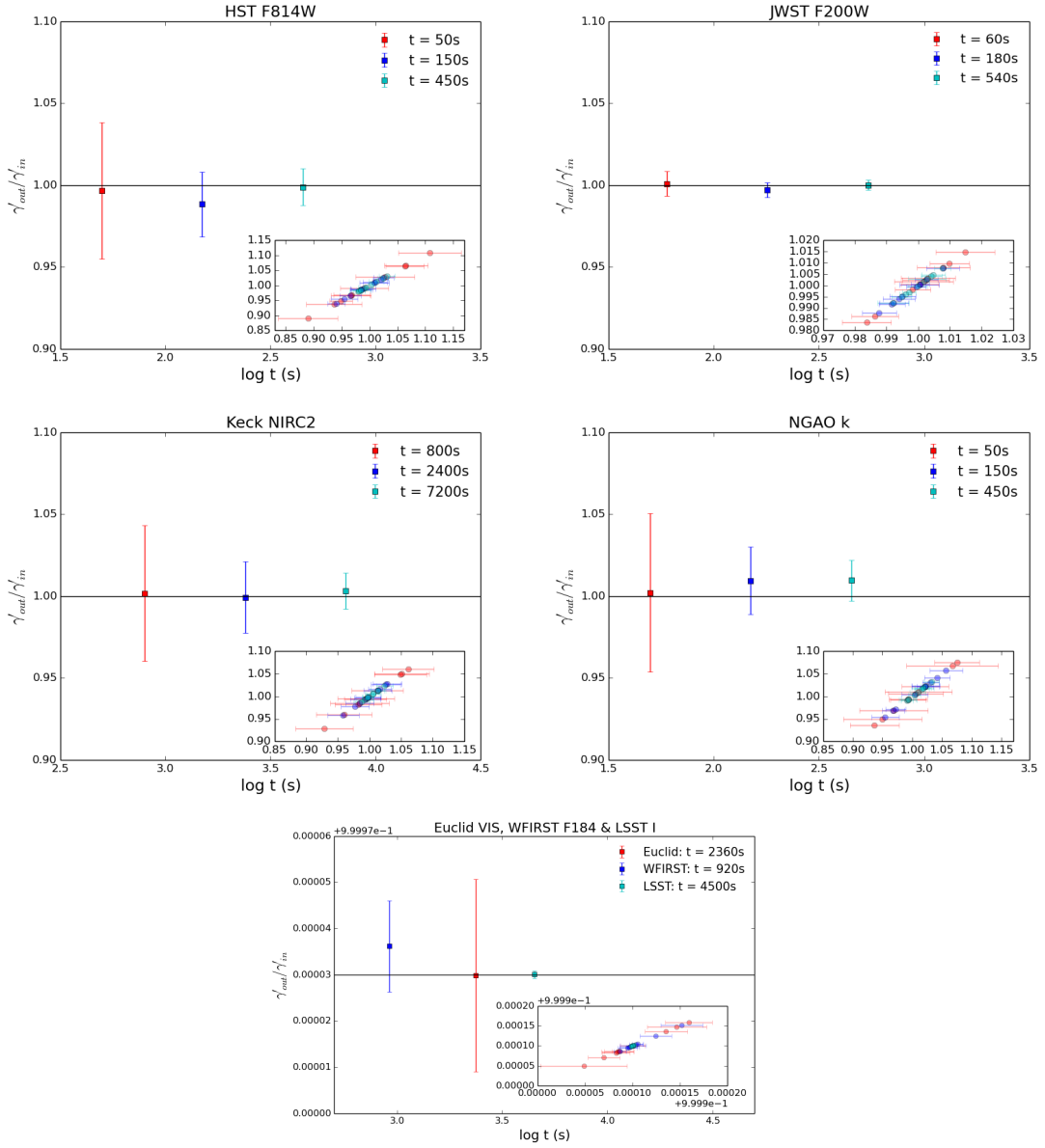


**Figure 10.** Same as Fig. 6, except that this figure is shown for the brighter lens system with 4 QSO images in the lens plane.